eChem
https://www.sciltp.com/journals/eChem



Article

Micropore-Confined P/O-Codoped Carbon Cages Stabilize Molybdenum Single-Atom Sites for Sulfur Conversion in Aluminum-Sulfur Batteries

Su Yang [1,2,†], Xiaolu Ma [2,†], Qian Bai [2], Runmin Li [2], Rui Yang [2], Jilin Li [2], Zhengbang Zhu [2], Weng-Chon (Max) Cheong [3], Wenxing Chen [2,*], Handong Jiao [1,*] and Shuqiang Jiao [4,*]

[1] Institute of Advanced Structure Technology, Beijing Institute of Technology, Beijing 100081, China
[2] Energy & Catalysis Center, School of Materials Science and Engineering, Beijing Institute of Technology, Beijing 100081, China
[3] Sino–Luso Joint Laboratory for Optoelectronics, Macao Institute of Materials Science and Engineering (MIMSE), Macau University of Science and Technology, Macao SAR 999078, China
[4] State Key Laboratory of Advanced Metallurgy, University of Science and Technology Beijing, Beijing 100081, China
* Correspondence: wxchen@bit.edu.cn (W.C.); jiaohandong_new@163.com (H.J.); sjiao@ustb.edu.cn (S.J.)
† These authors contributed equally to this work.

How To Cite: Yang, S.; Ma, X.; Bai, Q.; et al. Micropore-Confined P/O-Codoped Carbon Cages Stabilize Molybdenum Single-Atom Sites for Sulfur Conversion in Aluminum-Sulfur Batteries. *eChem* **2026**, *2*(2), 15. https://doi.org/10.53941/echem.2026.100015

Received: 25 July 2026
Revised: 26 October 2026
Accepted: 11 November 2026
Published: 23 November 2026

Abstract: Rechargeable aluminum–sulfur (Al–S) batteries combine earth-abundant electrodes with high theoretical energy density, but room-temperature operation remains constrained by slow sulfur conversion, migration of soluble aluminum polysulfides, and interfacial passivation by insulating discharge products. Here we construct a P/O-codoped microporous carbon cage that stabilizes atomically dispersed molybdenum sites (Mo-SA@P,O-PC) through a pore-matched confinement strategy. The microporous host is designed to retain the polyoxometalate precursor and to bring sulfur species into contact with P/O functionalities and Mo centers after pyrolysis. Electron microscopy, O 1s XPS, soft X-ray absorption spectroscopy, and Mo K-edge XAFS identify positively polarized, light-element-coordinated Mo single atoms without detectable Mo–Mo aggregation. In room-temperature $[AlCl_3]_{1.3}$[EMIM]Cl, the Mo-SA@P,O-PC/S cathode delivers approximately 550 mAh g^{-1} at 100 mA g^{-1}, whereas the metal-free control provides about 200 mAh g^{-1}. The electrode also maintains reversible operation as the current density is stepped from 200 to 500 mA g^{-1}, followed by substantial capacity recovery when the current is lowered. Cycling profiles remain similar through the 130th cycle at 500 mA g^{-1}, and the discharge capacity stabilizes near 130 mAh g^{-1} up to 180 cycles at 100 mA g^{-1} with high Coulombic efficiency. Operando Mo K-edge XAFS shows that the isolated Mo centers retain their first-shell coordination with small state-dependent changes in their electronic environment. These results support a proposed cooperative confinement, coordination, and catalysis mechanism for durable multistep sulfur conversion.

Keywords: Al-S battery; Mo single-atom sites; P,O-co-doped porous carbon; confinement

1. Introduction

Large-scale integration of renewable energy grid integration and long-duration energy storage urgently demand electrochemical storage technologies that combine low cost, intrinsic safety, and resource sustainability. Conventional lithium-ion batteries are constrained by limited lithium reserves and volatile raw material costs,

Copyright: © 2026 by the authors. This is an open access article under the terms and conditions of the Creative Commons Attribution (CC BY) license (https://creativecommons.org/licenses/by/4.0/).
Publisher's Note: Scilight stays neutral with regard to jurisdictional claims in published maps and institutional affiliations.

limiting their ability to meet the demands of gigawatt-scale stationary storage. This has driven widespread research into post-lithium battery chemistries based on earth-abundant elements. Aluminum stands out as a particularly promising anode material: it is the most abundant metallic element in the Earth's crust, is available at a very low raw-material cost, and delivers an ultrahigh theoretical volumetric capacity of 8046 mAh cm^{-3}, far exceeding that of metallic lithium. Benefiting from the three-electron redox chemistry of Al^{3+}, rechargeable aluminum batteries exhibit great potential for low-cost, high-energy-density storage, and have emerged as a vital candidate for next-generation battery systems [1–5]. Coupling a metallic aluminum anode with a sulfur cathode further elevates the material-level energy density and economic advantages. Sulfur is ultra-low-cost, environmentally benign, and offers an exceptionally high theoretical specific capacity of 1675 mAh g^{-1}. The resulting nonaqueous aluminum-sulfur (Al-S) battery system thus integrates the merits of both electrode materials, attracting sustained research attention over the past decade [6–10]. Nevertheless, room-temperature Al-S cells operating in Lewis-acidic chloroaluminate ionic liquids still face three interlocked fundamental challenges that hinder their practical development. First, elemental sulfur and the deeply discharged Al_2S_3 phase are electronically and ionically insulating, and their solid-liquid-solid conversion process readily causes interfacial passivation and incomplete sulfur utilization. Second, soluble aluminum polysulfides (AlPSs) intermediates formed during cycling can diffuse freely out of the cathode region, inducing continuous active sulfur loss and parasitic side reactions on the aluminum anode surface, namely the polysulfide shuttle effect. Third, the high charge density of trivalent Al species leads to strong electrostatic interactions with sulfur-containing intermediates, imposing large kinetic barriers on S–S bond cleavage, Al–S bond formation, and the reverse oxidation process. Collectively, these issues result in low sulfur utilization, wide voltage hysteresis, and rapid capacity fade, which represent the core bottlenecks restricting the performance of Al–S batteries [6–14].

Without altering the electrolyte chemistry of the benchmark room-temperature acidic $[AlCl_3]_{1.3}$[EMIM]Cl, mainstream cathode modification strategies can be broadly divided into two categories: physical confinement and catalytic promotion. On the one hand, hollow or hierarchically porous carbons, carbon nanotubes, graphene interlayers, and two-dimensional layered hosts are employed to shorten ion/electron transport distances and physically retard AlPS migration [8,15–22]. These carbonaceous hosts provide continuous electron pathways and pore space for sulfur accommodation, but the weak van der Waals interaction between nonpolar carbon and polar AlPSs cannot effectively suppress long-term shuttle behavior, nor can they accelerate the intrinsically sluggish sulfur conversion kinetics. On the other hand, polar or catalytically active species, including Co nanoparticles, TiN, Fe-based compounds, and Mo_2C, are introduced to strengthen chemical adsorption of intermediates and lower the reaction energy barrier for interfacial electron transfer [19,21,23–34]. While catalytic nanoparticles reduce kinetic hysteresis, their active sites are mostly exposed on the particle surface, leading to low atomic utilization. Moreover, nanoparticle catalysts are prone to pore blockage, phase reconstruction, and agglomeration during long-term cycling in corrosive chloroaluminate electrolytes, which reduces the density of durable active sites. As widely recognized in lithium–sulfur battery research, an optimal sulfur host must balance adsorption, diffusion, and catalytic turnover: excessively weak adsorption fails to suppress shuttling, whereas excessively strong adsorption immobilizes intermediates and blocks subsequent conversion [35–38]. Single-atom catalysts offer an ideal solution to this balance, featuring maximum atom utilization efficiency, well-defined local coordination environments, and tunable electronic states [39–45]. Atomically dispersed Co and Fe sites have already been applied in Al-S batteries, demonstrating effectiveness in reducing voltage hysteresis and prolonging cycling life [24–28,31,32]. Despite these advances, two critical unresolved questions remain, which fundamentally restrict the rational design of single-atom Al-S cathodes. First, high-temperature pyrolysis, the most common preparation route, inevitably causes metal atom migration and aggregation. How to suppress metal sintering while maintaining high site accessibility remains a synthetic challenge. Second, under the harsh conditions of strongly Lewis-acidic electrolyte and repeated sulfidation/desulfidation cycles, it remains unclear whether single-atom sites maintain their isolated structure, undergo reversible electronic modulation, or suffer irreversible reconstruction. Post-synthesis electron microscopy or the absence of XRD diffraction peaks can only provide static structural information and cannot directly verify the working-state structure and dynamic evolution of active sites during electrochemistry.

Here, we propose a continuous "precursor confinement–site confinement–sulfur-species confinement" triple-confinement strategy based on pore-size matching. Sucrose/$NaHCO_3$-derived microporous carbon (micro-PC) possesses a concentrated ultramicropore distribution in the subnanometer to 1 nm range, which is dimensionally matched to polyoxometalate (POM) clusters. During impregnation, precursor uptake into the accessible porous network provides the basis for the proposed confinement strategy [46]; during subsequent confined pyrolysis, the P/O-codoped carbon walls anchor and stabilize the isolated Mo centers, inhibiting long-range migration and aggregation. After sulfur loading, the same ultramicropores further confine AlPS intermediates, shorten their diffusion distance to catalytic sites, and enable efficient adsorption-conversion turnover. We employ a combination

of HAADF-STEM, soft X-ray absorption spectroscopy, ex situ and operando Mo K-edge XAFS, paired with a metal-free PC/S control sample, to distinguish directly observed structural evidence from mechanistic inferences, and to establish the correlation among site structural stability, dynamic electronic response, and sulfur conversion kinetics. This work not only provides a feasible synthetic route for stable Mo single-atom carbon hosts, but also provides selected-state Mo K-edge characterization of this host in the Al–S system; the electrochemical-state metadata are specified in the Supporting Information.

2. Materials and Methods

2.1. Materials

Sucrose ($C_{12}H_{22}O_{11}$, 99.9%), sodium bicarbonate ($NaHCO_3$, 99.8%), and phosphomolybdic acid (PMo_{12}, 99%) were purchased from Shanghai Aladdin Biochemical Technology Co., Ltd. (Shanghai, China). Sulfuric acid (H_2SO_4, analytical grade) and dilute hydrochloric acid (10%) were obtained from Tianjin Tianli Chemical Reagent Co., Ltd. (Tianjin, China). Unless otherwise stated, all chemicals were used as received.

2.2. Preparation of Catalysts

Microporous carbon was prepared by a carbonization/activation route using sucrose as the carbon source. Sucrose and $NaHCO_3$ were thoroughly ground at a mass ratio of 1:4, heated under Ar at 10 °C min^{-1}, and held at 400 °C and 900 °C for 1h at each temperature. The product was washed with aqueous HCl, filtered, and dried at 70 °C to obtain PC. PC was mixed with 20 mL of 1 mM PMo_{12} solution, stirred for 1 h, filtered, washed until the filtrate was neutral, and dried to obtain POM@micro-PC. POM@micro-PC was heated under Ar to 900 °C at 5 °C min^{-1} and held for 2 h for confined pyrolysis. After cooling, the solid was treated with 0.5 M H_2SO_4 at 80 °C for 24 h, followed by filtration, washing, and drying at 70 °C.

2.3. Materials Characterization

The morphology of the samples was characterized by FE-SEM (JSM-6700F, accelerating voltage of 5 kV), HRTEM (JEM-2010, accelerating voltage of 200 kV, JEOL Ltd., Tokyo, Japan), and high-angle annular dark-field scanning transmission electron microscopy (JEOL JEM-ARM200F TEM, accelerating voltage of 200 kV, JEOL Ltd., Tokyo, Japan). A 30 mrad convergence angle was used to record the HAADF-STEM images, with the inner and outer collection angles of 68 and 280 mrad, respectively. EDS data were collected by an X-MaxN100TLE detector (Oxford Instruments NanoAnalysis, High Wycombe, UK). The crystalline structures of as-synthesized materials were measured by XRD on a Rigaku D/Max Ultima IV diffractometer with filtered Cu-Kα radiation (λ = 1.5418 Å) (Rigaku Corporation, Tokyo, Japan). Fourier transform infrared (FTIR) spectra were obtained on a Brucker Vector 22 FTIR spectrometer (Bruker Optics GmbH & Co. KG, Ettlingen, Germany). The thermal stability of materials was analyzed by using a thermogravimetric analyzer (TG-MS, SETARAM, SETARAM, Caluire, France). Elemental electron binding energy was measured by X-ray photoelectron spectroscopy (XPS; ESCALAB 250XI, SETARAM, Caluire, France). Ionic (Mo) concentration was analyzed by inductively coupled plasma-optical emission spectroscopy (ICP-OES; Avio 200, PerkinElmer, Singapore). Raman spectra were obtained on a HORIBA spectrometer (PerkinElmer, Singapore) with excitation by a laser of 532 nm. UV–vis spectrum was recorded on a TU-1950 spectrophotometer (Beijing Purkinje General Instrument Co., Ltd., Beijing, China). Nitrogen adsorption/desorption experiments were performed at 77K on a Micromeritics ASAP 2020 equipment (Micromeritics Instrument Corp., Norcross, GA, USA). Prior to the adsorption measurements, thoroughly washed samples underwent solvent exchange with acetone followed by hexane at least five times, respectively, and dried in a pre-heated 85 °C oven for 30 min. Resulting powder was then activated for Brunauer–Emmett–Teller (BET) measurement at 150 °C for 2 h. The BET model was used for the specific surface area determination. T-plot method was used to obtain the micropore volume. Total pore volume was obtained by Gurvitsch's rule at P/P_0=0.99. In order to calculate micropore size distributions, Non-Local Density Functional Theory (NLDFT) was employed to analyze the low pressure adsorption isotherms by assuming slit-like carbon pore geometry.

2.4. Soft XAS Measurements

The C K-edge and S L-edge XANES spectra were collected at beamline BL12B of the National Synchrotron Radiation Laboratory (NSRL), China. Samples were deposited on double-sided conductive carbon tape. P incorporation in the present data set is evaluated by elemental mapping and P 2p XPS.

2.5. Ex Situ XAFS Measurements

Mo K-edge XAFS data were collected at beamline BL14W1 of the Shanghai Synchrotron Radiation Facility (SSRF; 3.5 GeV, maximum current 250 mA). The incident beam was monochromatized using a Si (111) double-crystal monochromator. Solid samples were mounted on Al holders and sealed with Kapton film. Fluorescence-mode spectra were acquired with a Lytle detector, and the energy was calibrated using Mo foil.

2.6. Electrochemical Measurements

The cathode slurry consisted of 60 wt% S@host composite, 30 wt% Super P, and 10 wt% PVDF. The slurry was coated on Mo-foil current collectors and dried under vacuum. A nominal sulfur feed fraction of 60 wt% corresponds to a nominal sulfur fraction of 0.60 × 0.60 = 0.36, or 36 wt%, in the dry coating. Nominal feed fractions are distinguished from measured sulfur contents; the new thermogravimetric results are given in Figure S18. Swagelok-type cells were assembled in an Ar glovebox using Al foil as the anode, glass fiber as the separator, and acidic $[AlCl_3]_{1.3}$[EMIM]Cl ($AlCl_3$: [EMIM]Cl = 1.3:1) as the electrolyte. Galvanostatic cycling was performed at room temperature over 0.01–1.9 V versus Al^{3+}/Al. CV and EIS were measured with an electrochemical workstation; EIS was collected from 100 kHz to 0.01 Hz.

3. Results and Discussion

3.1. Pore-Matched Confined Synthesis

The synthesis strategy of Mo-SA@P,O-PC is schematically illustrated in Figure 1a. In this approach, sucrose serves as the carbon source, while $NaHCO_3$ functions as a pore-generating and activating agent through gas release during the staged carbonization process, resulting in the formation of a carbon host enriched with narrow micropores. These microporous channels provide the design basis for pore-assisted retention of polyoxometalate (POM) precursors, following the uptake route established for the unpyrolyzed precursor/carbon material [46]. During subsequent high-temperature pyrolysis, the confined pores effectively restrict precursor migration and diffusion, thereby suppressing the collision and aggregation of Mo species. After confined pyrolysis at 900 °C, the precursor-derived species are converted into atomically dispersed Mo sites anchored within the P/O-codoped carbon framework. The product was then acid-washed soluble residues and unstable surface species. This pore-confinement strategy extends the conventional oxide-support-mediated atomic trapping mechanism toward carbon-based nanoscale confinement systems, where spatial restriction and local anchoring synergistically stabilize isolated Mo active sites while preventing metal aggregation [47].

The structural evolution of the carbon framework during each synthesis stage was first investigated by scanning electron microscopy (SEM). As shown in Figures S1–S3, the micro-PC, POM@micro-PC, and Mo-SA@P,O-PC samples retain interconnected porous architectures after precursor impregnation, high-temperature pyrolysis, and acid treatment, demonstrating the structural robustness of the carbon framework throughout the synthesis process. High- and low-magnification SEM images further reveal that Mo-SA@P,O-PC possesses a continuous porous carbon network with abundant open channels (Figure 1b,c), which can facilitate active-site exposure and mass transport. Transmission electron microscopy (TEM) observations further confirm the ultrathin and highly porous morphology of the carbon matrix (Figures S4–S6). Importantly, high-resolution TEM images show no detectable lattice fringes associated with Mo-based crystalline phases, suggesting the absence of large Mo nanoparticles or crystalline Mo aggregates. Preliminary evidence suggests that molybdenum species exist in an ultrafine dispersed state within the carbon skeleton. The elemental distribution was further examined by energy-dispersive spectroscopy (EDS) mapping. As shown in Figure 1d, the C, Mo, P, and O signals are uniformly distributed throughout the carbon framework without observable microscale segregation, indicating homogeneous incorporation of Mo and heteroatom species. X-ray diffraction (XRD) patterns of micro-PC, POM@micro-PC, and Mo-SA@P,O-PC exhibit only broad diffraction features associated with turbostratic carbon, while no characteristic diffraction peaks corresponding to metallic Mo, MoO_2, Mo_2C, or MoS_2 are detected (Figure 1e), further excluding the formation of crystalline Mo-containing phases. To directly visualize the atomic dispersion of Mo species, aberration-corrected high-angle annular dark-field scanning transmission electron microscopy (HAADF-STEM) was performed. As shown in Figure 1f, numerous isolated high-Z-contras bright spots are uniformly distributed across the carbon matrix, corresponding to individual Mo atoms anchored within the carbon framework. Statistical analysis of the atomic contrast features reveals that the apparent diameters are concentrated in the range of 0.14–0.15 nm (Figures 1g and S7), confirming the atomic-level dispersion of Mo species without detectable clustering or nanoparticle formation. ICP analysis of the final, pyrolyzed and acid-washed sulfur-free

Mo-SA@P,O-PC host gives Mo and P contents of 3.37 and 0.10 wt%, respectively (Table S1). These are total elemental loadings; the dispersion of Mo is assessed separately by microscopy and XAFS.

Nitrogen adsorption–desorption measurements were further employed to monitor the evolution of the pore structure during precursor confinement and conversion. The pristine micro-PC exhibits a high Brunauer-Emmett-Teller (BET) surface area of 1306.4 $m^2 g^{-1}$, which decreases to 319.3 $m^2 g^{-1}$ after POM loading due to precursor occupation and partial blocking of accessible micropores (Figure S8). After confined pyrolysis and acid washing, the surface area recovers to 1102.2 $m^2 g^{-1}$, indicating the reconstruction and reopening of the pore network after precursor conversion and removal of unstable species. The pronounced micropore distribution centered at approximately 1.1 nm further confirms the presence of narrow confinement channels, which provide a suitable spatial environment for precursor immobilization and subsequent stabilization of isolated Mo sites. Together with the preceding unpyrolyzed-material study [46], these results are consistent with precursor uptake, partial pore occupation, and reopening after thermal conversion. Pore-size matching is a design rationale; The stable porous carbon framework enables homogeneous precursor accommodation within narrow micropores, while spatial restriction during pyrolysis suppresses Mo migration and aggregation. Consequently, atomically dispersed Mo sites are successfully stabilized within the P/O-codoped carbon matrix.

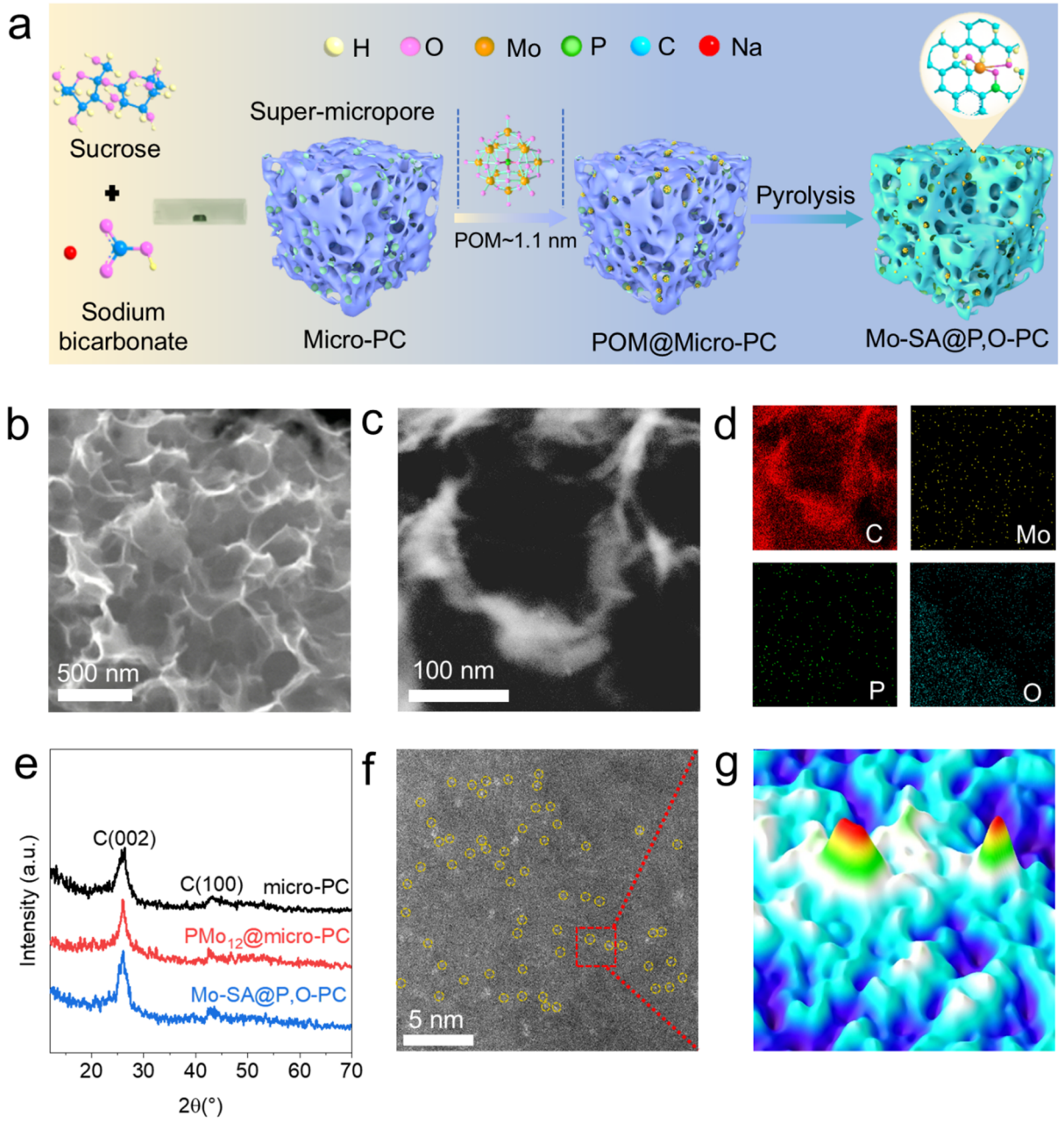

Figure 1. Pore-matched synthesis and structural characterization of Mo-SA@P,O-PC. (**a**) Schematic illustration of micro-PC formation, confinement of a ca.1.1 nm POM precursor, and confined pyrolysis. (**b**,**c**) SEM images showing the connected porous carbon framework and open transport pathways. (**d**) Elemental maps of C, Mo, P,

and O. (**e**) XRD patterns of micro-PC, POM@micro-PC, and Mo-SA@P,O-PC. (**f**) HAADF-STEM image showing isolated high-Z spots assigned to atomically dispersed Mo. (**g**) The intensity profiles highlighted along the red dashed square in (**f**). The red peaks correspond to the metal atoms with strong Z-contrast signals, and the blue background represents the support substrate.

3.2. Electronic Structure and Local Coordination of Mo Single Atoms

The electronic structure and coordination environment of Mo single atoms were systematically investigated by combining synchrotron-based X-ray absorption spectroscopy (XAS), Raman spectroscopy, and X-ray photoelectron spectroscopy (XPS). The C K-edge XAS spectra exhibit characteristic π*(C=C) and σ*(C–C) transitions associated with the conjugated carbon framework, together with additional features related to oxygen-containing functionalities and carbon defects (Figure 2a). The O 1s spectra provide a direct view of the oxygen-containing coordination environment (Figure 2b). The O 1s spectrum of PC is dominated by C–OH/C–O–C species. After POM infiltration, additional Mo–O and P–O contributions appear, and these components remain detectable in Mo-SA@P,O-PC after confined pyrolysis. The result supports the formation of a P/O-rich local environment around the dispersed Mo centers. The variation in the intensity ratio between D and G bands in Raman spectra among micro-PC, POM@micro-PC, and Mo-SA@P,O-PC (Figure S9) [48] reflects the evolution of defect structures and edge environments during precursor conversion. High-resolution C 1s, Mo 3d, and P 2p XPS spectra further confirm the incorporation of Mo, O, and P species into the carbon framework (Figure S10). The S L-edge spectrum of the sulfur-loaded composite is provided separately in Figure S16, where the sulfur-related features confirm a chemically nonuniform sulfur environment after loading.

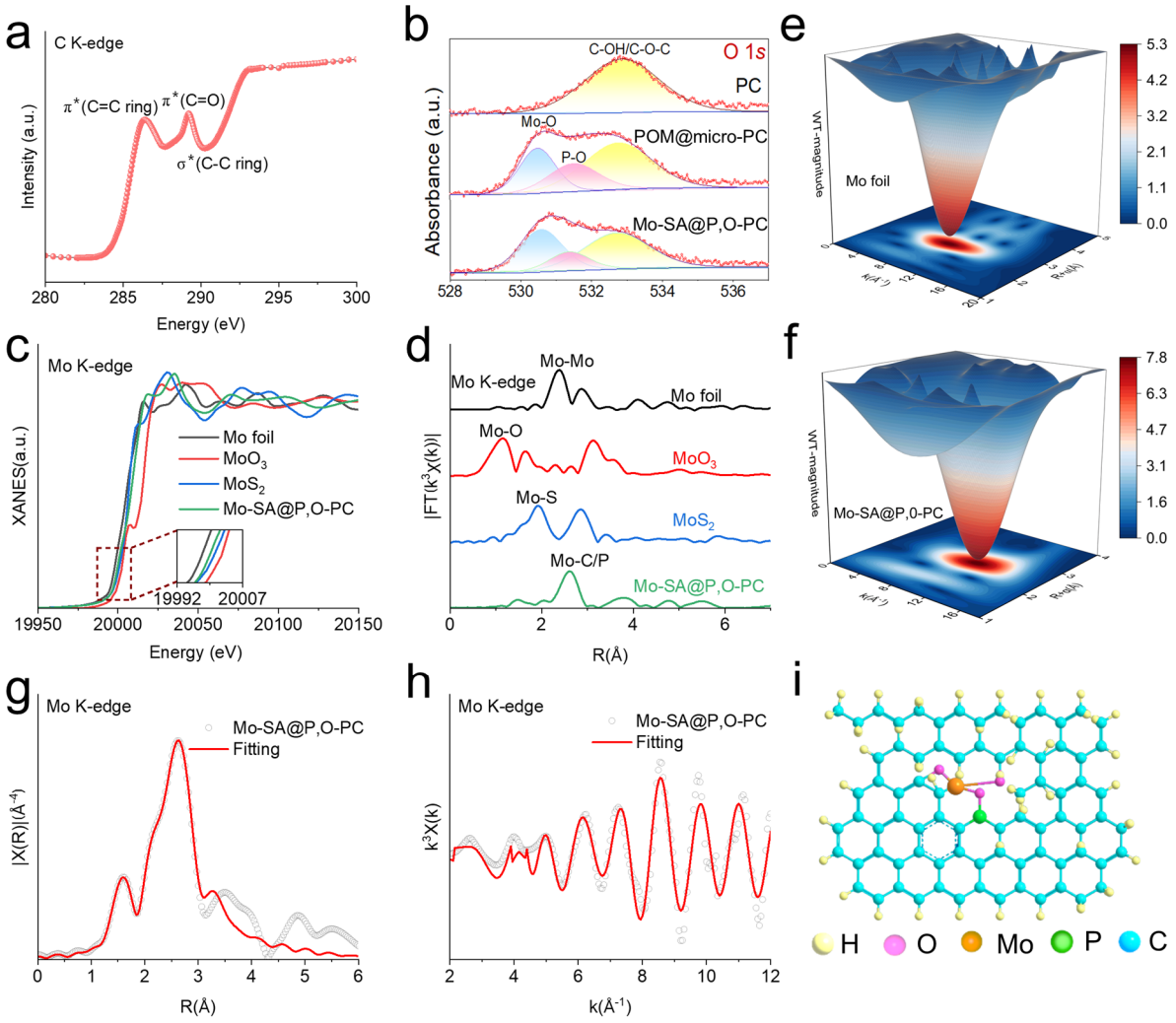

Figure 2. Electronic structure and local coordination of Mo-SA@P,O-PC. (**a**) C K-edge XAS. (**b**) O 1s XPS spectra of PC, POM@micro-PC, and Mo-SA@P,O-PC. The yellow, pink, and light-blue shaded areas represent the fitted C–OH/C–O–C, P–O, and Mo–O components, respectively. (**c**) Mo K-edge XANES of Mo-SA@P,O-PC and the Mo foil, MoO_3, and MoS_2 references. (**d**) Fourier-transformed EXAFS, where the principal Mo-SA@P,O-PC

contribution is tentatively assigned to a light-element first-shell Mo–X environment. (**e**,**f**) Wavelet-transform EXAFS of Mo foil and Mo-SA@P,O-PC. (**g**,**h**) R-space and k-space fits. (**i**) Proposed P/O/C-containing Mo model; the ligand configuration is not uniquely resolved.

To identify the electronic configuration and local coordination environment of Mo centers, synchrotron Mo K-edge XANES and EXAFS measurements were performed. The Mo K-edge XANES spectrum of Mo-SA@P,O-PC shows an absorption edge located between metallic Mo foil and MoO_3 references (Figure 2c), indicating that Mo species exist in a partially oxidized state rather than a metallic state. The k^3-weighted Fourier-transformed EXAFS spectrum exhibits a dominant first-shell coordination peak at low radial distance, consistent with coordination to light-element ligands, provisionally described as Mo–X (X=O/C/P), while no detectable Mo–Mo scattering contribution comparable to Mo foil is observed (Figure 2d). The wavelet transform (WT)-EXAFS analysis provides further confirmation of the atomic dispersion of Mo species. Unlike metallic Mo foil, which exhibits a characteristic high-wavevector Mo–Mo scattering signal, Mo-SA@P,O-PC displays only a low-k first-shell Mo–X scattering feature (Figure 2e,f), with no resolved metallic-Mo-like contribution in these spectra. Quantitative EXAFS fitting in both R-space and k-space shows good agreement between experimental spectra and theoretical simulations, while q-space fitting provides additional phase-sensitive verification of the coordination configuration (Figures 2g,h and S11). The quantitative EXAFS fitting parameters are summarized in Table S2. The same analysis protocol accurately recovers Mo–Mo coordination in the Mo-foil reference (Figure S12), strengthening the assignment of the target sample to an isolated light-element-coordinated Mo configuration. Compared with single-dimensional spectral interpretation, the combination of multiple XAS analyses provides more comprehensive evidence for accurately identifying atomic-scale structures in single-atom catalysts [49]. Based on these results, a three-dimensional (3D) atomic interface structure model of Mo-SA@P,O-PC was constructed (Figure 2i).

3.3. Single-Atom Microenvironment Enhances Sulfur Conversion

Two-electrode Al–S cells were assembled using Mo-SA@P,O-PC/S or PC/S as the cathode, Al foil as the anode, a glass-fiber separator, and acidic $[AlCl_3]_{1.3}$[EMIM]Cl electrolyte at room temperature. The photograph and exploded-view schematic in Figure 3a show the practical PTFE cell body and the internal sequence of sulfur cathode, electrolyte-soaked separator, and Al anode. Both sulfur-loaded composites were prepared with a nominal sulfur feed fraction of 60 wt%, and the two cathodes were evaluated with the same electrode formulation and cell protocol. This paired design compares the integrated POM-derived Mo/P/O-containing host with the metal-free carbon reference; it does not isolate the contribution of Mo from concurrent changes in heteroatom chemistry and pore structure. Sulfur-free PC and Mo-SA@P,O-PC produce only weak background currents without the characteristic sulfur-conversion peaks (Figure S17), confirming that the dominant faradaic response of the complete cathodes originates from sulfur chemistry. The difference is already evident in the CV curves. The CV curves were recorded at 0.2 mV s^{-1} (Figure 3b). The galvanostatic profiles at 100 mA g^{-1} provide a quantitative comparison. Mo-SA@P,O-PC/S reaches a discharge capacity of approximately 550 mAh g^{-1}, whereas PC/S is limited to about 200 mAh g^{-1} (Figure 3c). The longer conversion plateau of the single-atom cathode indicates that a substantially larger fraction of sulfur remains electrochemically accessible. EIS offers an independent view of the same improvement. The Mo-containing electrode exhibits a smaller high- and mid-frequency semicircle than PC/S (Figure 3d), which is consistent with faster interfacial charge transfer and reduced accumulation of poorly conducting products.

The single-atom microenvironment continues to function when the reaction rate is increased. Charge and discharge profiles retain their characteristic shape from 200 to 500 mA g^{-1} (Figure 3e). The corresponding rate sequence shows a gradual capacity decrease with increasing current density, followed by clear recovery when the current returns to the lower rate (Figure 3f). This recovery is important because it shows that the temporary loss at high current is mainly kinetic rather than the result of irreversible sulfur depletion. At 500 mA g^{-1}, the 30th, 35th, 50th, 80th, and 130th profiles remain closely grouped (Figure 3g), indicating that the polarization changes only moderately during extended operation. In a separate test, the cell retains at 100 mA g^{-1} maintains a discharge capacity close to 130 mAh g^{-1} up to 180 cycles, while the Coulombic efficiency remains high (Figure 3h). The influence of sulfur loading on electrochemical behavior was additionally investigated by varying the nominal sulfur feed fraction from 30 to 70 wt% (Figure S15). The results reveal that increasing sulfur input does not continuously improve reversible capacity; instead, excessive sulfur loading leads to increases the electrochemically accessible sulfur fraction. The observed trend indicates that overly high sulfur incorporation may exceed the effective accommodation capability of the porous framework, resulting in pore occupation, electronically isolated sulfur domains, or increased parasitic reactions. Therefore, optimizing the balance between

sulfur loading and accessible catalytic interfaces is essential for achieving efficient sulfur utilization. Viewed together, these results show that the Mo/P/O site ensemble improves the amount of sulfur that can participate, sustains conversion over a broad rate range, and limits progressive kinetic deterioration. A comparison with reported aluminum-based battery cathodes is provided in Table S3.

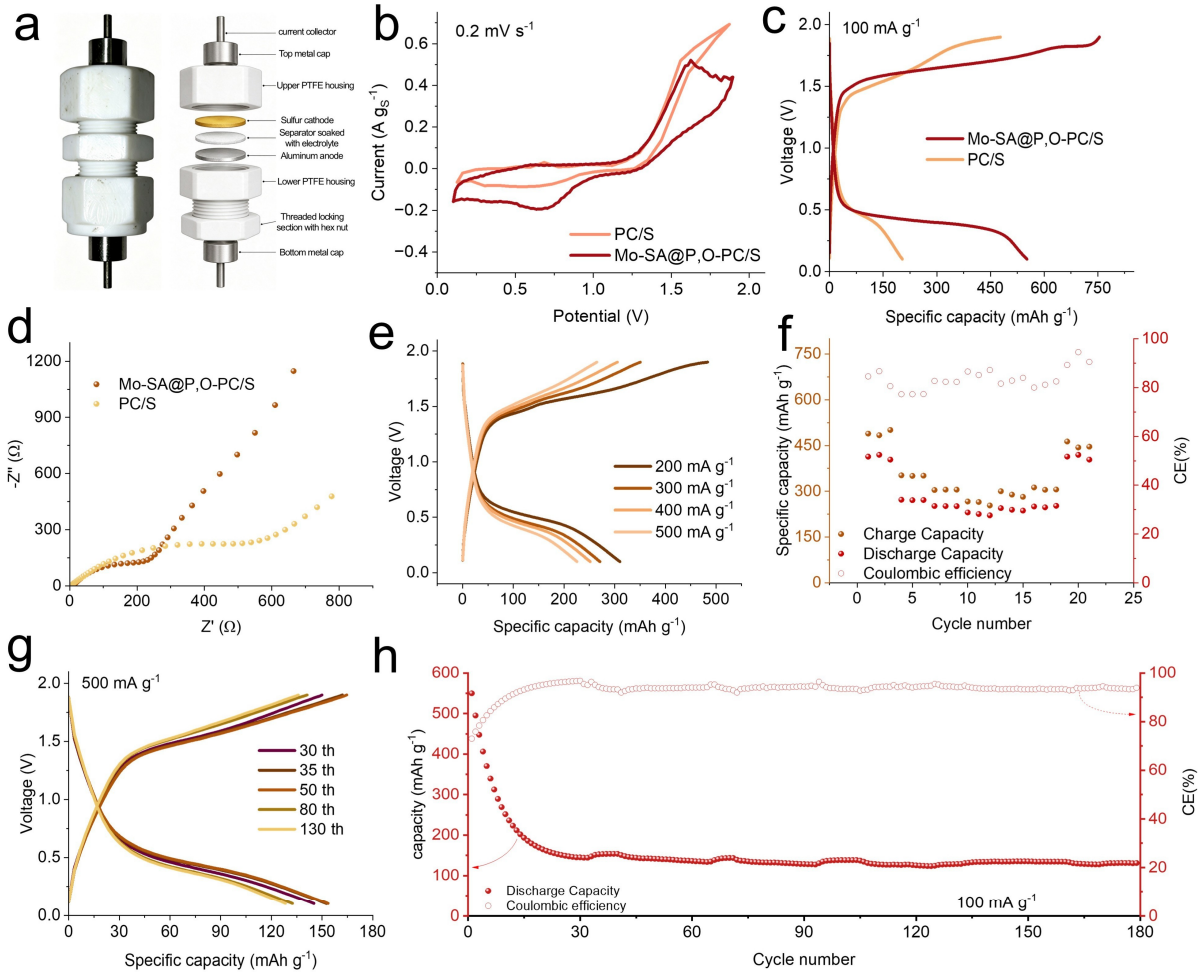

Figure 3. Electrochemical behavior of Mo-SA@P,O-PC/S and PC/S in room-temperature $[AlCl_3]_{1.3}$[EMIM]Cl. Both sulfur-host composites were prepared using a nominal sulfur feed fraction of 60 wt%. (**a**) Photograph and exploded-view schematic of the two-electrode Al–S cell. (**b**) CV curves at 0.2 mV s^{-1}. (**c**) Galvanostatic charge/discharge profiles at 100 mA g^{-1}. (**d**) Nyquist plots. (**e**) Galvanostatic profiles of Mo-SA@P,O-PC/S at 200, 300, 400, and 500 mA g^{-1}. (**f**) Rate performance and Coulombic efficiency during stepwise current-density changes between 200 and 500 mA g^{-1}. (**g**) Selected profiles at 500 mA g^{-1} for the 30th, 35th, 50th, 80th, and 130th cycles. (**h**) Long-term cycling at 100 mA g^{-1} up to 180 cycles.

3.4. Operando Mo K-Edge XAFS and Working-State Response

To elucidate the working-state behavior of isolated Mo sites during sulfur conversion, operando Mo K-edge X-ray absorption spectroscopy (XAFS) was performed under practical Al–S electrochemical conditions. Operando XAFS enables direct monitoring of the structural and electronic evolution of Mo centers during electrochemical operation, providing insight into whether the confined single-atom sites remain structurally stable and actively respond to the reaction environment. The three-dimensional operando XANES map exhibits reproducible spectral evolution upon electrochemical polarization (Figure 4a), demonstrating that the electronic environment of Mo centers dynamically responds to the battery operating state. The corresponding Mo K-edge XANES spectra collected at open circuit potential (OCP), 1.45 V, and 1.50 V show subtle but distinguishable variations in edge position and white-line intensity compared with reference compounds (Figure 4b). Linear calibration of edge energy with oxidation state (Figure 4c) shows that the average oxidation state of Mo is 1.93 at 1.45 V and 1.96 at 1.50 V, which is close to the oxidation state of MoS_2. The Fourier-transformed EXAFS spectra collected at OCP, 1.45 V, and 1.50 V are dominated by the first-shell Mo–X coordination contribution, with no detectable Mo–Mo scattering feature comparable to that of metallic Mo foil (Figure 4d). The k-space and R-space fits reproduce the

spectra collected under electrochemical polarization (Figure 4e,f), while the OCP fit and the q-space fits of the polarized states provide independent consistency checks (Figures S13 and S14). Furthermore, wavelet-transform EXAFS analysis provides additional evidence for the absence of Mo aggregation, as all electrochemical states exhibit a low-k first-shell signal without the high-k contribution characteristic of Mo–Mo coordination (Figure 4g–i).

These results reveal a defining feature of the confined Mo single-atom sites: structural robustness accompanied by electronic adaptability. Based on the electrochemical results and operando XAFS analysis, a dynamic catalytic microenvironment is proposed for Mo-SA@P,O-PC/S. The microporous carbon framework confines sulfur species within nanoscale domains, the P/O functionalities provide a polar interface for regulating sulfur-containing intermediates, and isolated Mo centers act as electronically responsive reaction nodes during sulfur conversion. This cooperative confinement strategy enables enhanced sulfur utilization and long-term electrochemical stability by integrating structural stabilization with dynamic interfacial regulation.

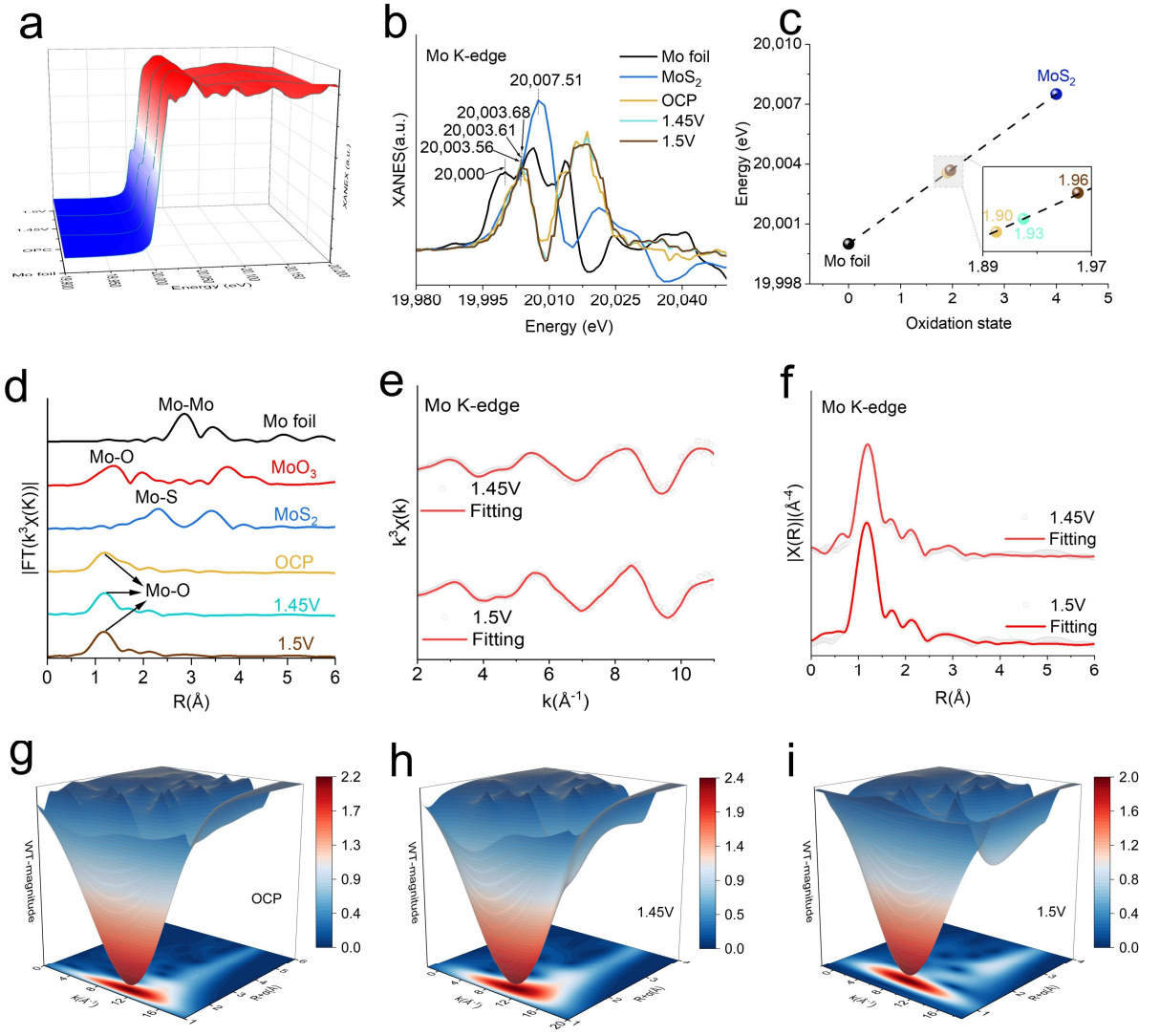

Figure 4. Operando Mo K-edge XAFS of Mo-SA@P,O-PC under Al–S electrochemical polarization. (**a**) Three-dimensional XANES evolution. Schematic local-potential landscape of the polar microporous coordination environment. The color represents the HAADF signal intensity, where the red peaks correspond to the metal atoms/clusters with strong Z-contrast signals, and the blue background represents the support substrate. (**b**) XANES spectra at OCP, 1.45 V, and 1.50 V with reference compounds. (**c**) Edge-energy calibration. (**d**) Fourier-transformed EXAFS. (**e**) k-space fitting at 1.45 and 1.50 V. (**f**) R-space fitting at the same potentials. (**g–i**) Wavelet-transform EXAFS maps at OCP, 1.45 V, and 1.50 V. (**g**) The 3D topographic rendering converted from the HAADF-STEM image (**f**). The color represents the HAADF signal intensity, where the red peaks correspond to the metal atoms with strong Z-contrast signals, and the blue background represents the support substrate.

3.5. Confinement–Coordination–Catalysis Relationship

The data motivate a proposed three-level structure–function relationship. Geometric confinement originates from the connected microporous carbon skeleton. The microscopy results and the pore-occupation/reopening sequence in Figures 1 and S1–S8 show that the framework can immobilize the POM precursor without sacrificing access to the pore network. Coordination confinement emerges during pyrolysis. HAADF-STEM, O 1s XPS, and multi-domain XAFS in Figures 1f, 2 and S9–S12 identify positively polarized Mo single atoms held within a P/O/C-rich environment. The third level appears during electrochemical operation. Figure 3 shows that this local structure increases sulfur utilization, enables capacity recovery after high-rate operation, and suppresses the growth of interfacial resistance. The sulfur-free controls in Figure S17 exclude a substantial redox contribution from the host itself. Finally, Figures 4 and S13–S14 show that the isolated Mo centers adapt electronically while a first-shell spectral feature is retained at the sampled states.

These three levels cooperate within the same nanoscale reaction domain. The micropores retain sulfur species and shorten their diffusion distance; P/O functionalities may modify the interfacial polarity and adsorption of AlPS; and Mo is proposed to participate in interfacial charge redistribution. The PC/S control supplies physical confinement but lacks the complete P/O/Mo site ensemble, explaining its lower discharge capacity and larger impedance under the reported comparison conditions. Mo-SA@P,O-PC therefore operates as an integrated catalytic microenvironment rather than as a simple sulfur container. This design principle—spatially confining both the precursor and the reaction while preserving electronic flexibility at the atomic site—offers a broadly applicable route to durable single-atom cathodes.

4. Conclusions

In summary, a pore-matched confinement strategy was developed to construct P/O-codoped microporous carbon cages containing atomically dispersed Mo centers for room-temperature Al–S batteries. The subnanometer pore network confines the POM precursor during pyrolysis, and the resulting P/O/C environment stabilizes positively polarized Mo single atoms while preserving space for sulfur accommodation. Microscopy, O 1s XPS, soft XAS, and Mo K-edge XAFS provide mutually consistent structural evidence. Using a nominal sulfur feed fraction of 60 wt%, Mo-SA@P,O-PC/S delivers approximately 550 mAh g^{-1} at 100 mA g^{-1}, compared with approximately 200 mAh g^{-1} obtained from PC/S under the same conditions. The electrode retains reversible charge/discharge behavior over 200 to 500 mA g^{-1}, recovers capacity when the current is lowered, and maintains stable profiles during extended cycling. Operando XAFS links this behavior to Mo centers that preserve their local coordination with small changes in the electronic environment at the sampled states. The study therefore demonstrates how geometric confinement and a chemically active single-atom microenvironment can be combined to improve multistep sulfur conversion in a multivalent metal–sulfur battery.

Supplementary Materials

The additional data and information can be downloaded at: https://media.sciltp.com/articles/others/2611231431373777/eChem-26070246-SI.pdf. The Supporting Information contains detailed synthesis and characterization procedures; Figures S1–S3, SEM images; Figures S4–S6, TEM/HRTEM images; Figure S7, statistics of isolated high-Z spots; Figure S8, N2 sorption and pore-size distributions; Figure S9, Raman spectra; Figure S10, high-resolution XPS spectra; Figures S11–S14, EXAFS fitting results; Figure S15, sulfur-feed comparison; Figure S16, S L-edge XAS; Figure S17, sulfur-free-host CV controls. Additional characterization and electrochemical comparisons are provided in Figures S18–S25, with quantitative parameters and literature comparisons in Tables S1–S4 [50–56].

Author Contributions

S.Y.: conducted the experiments and performed the characterization; X.M.: wrote the manuscript; Q.B. and R.L.: formal analysis; R.Y., J.L. and Z.Z.: data curation; W.-C.C., W.C., H.J. and S.J.: conceived the project. All authors have read and agreed to the published version of the manuscript.

Funding

We acknowledge financial support from the Southern Marine Science and Engineering Guangdong Laboratory (Zhuhai) (Nos. SML2023SP242, SML2024P007), National Natural Science Foundation of China (Nos. 52274291, 52204305, 92475202), Joint Science Project of Gansu Province (24JRRA822), Open Fund of the State

Key Laboratory of Advanced Metallurgy (No. K25-04), and Beijing Institute of Technology Research Fund Program for Young Scholars (No. 1740011182102).

Institutional Review Board Statement

Not applicable.

Informed Consent Statement

Not applicable.

Data Availability Statement

All the necessary data is available in the main text and Supplementary Materials. The data is also available on request from the authors.

Conflicts of Interest

The authors declare no conflict of interest.

Use of AI and AI-Assisted Technologies

During the process of writing this article, we utilized ChatGPT (OpenAI) for language polishing. After using this tool, we carefully reviewed and revised the content as necessary, and assume full responsibility for the published content.

References

1. Dunn, B.; Kamath, H.; Tarascon, J.M. Electrical Energy Storage for the Grid: A Battery of Choices. *Science* **2011**, *334*, 928–935. https://doi.org/10.1126/science.1212741.
2. Elia, G.A.; Marquardt, K.; Hoeppner, K.; et al. An Overview and Future Perspectives of Aluminum Batteries. *Adv. Mater.* **2016**, *28*, 7564–7579. https://doi.org/10.1002/adma.201601357.
3. Lin, M.C.; Gong, M.; Lu, B.; et al. An ultrafast rechargeable aluminium-ion battery. *Nature* **2015**, *520*, 324–328. https://doi.org/10.1038/nature14340.
4. Yang, H.; Li, H.; Li, J.; et al. The Rechargeable Aluminum Battery: Opportunities and Challenges. *Angew. Chem. Int. Ed.* **2019**, *58*, 11978–11996. https://doi.org/10.1002/anie.201814031.
5. Faegh, E.; Ng, B.; Hayman, D.; et al. Practical assessment of the performance of aluminium battery technologies. *Nat. Energy* **2021**, *6*,21–29. https://doi.org/10.1038/s41560-020-00728-y. Correction in *Nat. Energy* **2021**, *6*, 450.
6. Cohn, G.; Ma, L.; Archer, L.A. A novel non-aqueous aluminum sulfur battery. *J. Power Sources* **2015**, *283*, 416–422. https://doi.org/10.1016/j.jpowsour.2015.02.131.
7. Gao, T.; Li, X.; Wang, X.; et al. A Rechargeable Al/S Battery with an Ionic-Liquid Electrolyte. *Angew. Chem. Int. Ed.* **2016**, *55*, 9898–9901. https://doi.org/10.1002/anie.201603531.
8. Yu, X.; Manthiram, A. Electrochemical Energy Storage with a Reversible Nonaqueous Room-Temperature Aluminum–Sulfur Chemistry. *Adv. Energy Mater.* **2017**, *7*, 1700561. https://doi.org/10.1002/aenm.201700561.
9. Yang, H.; Yin, L.; Liang, J.; et al. An Aluminum–Sulfur Battery with a Fast Kinetic Response. *Angew. Chem. Int. Ed.* **2018**, *57*, 1898–1902. https://doi.org/10.1002/anie.201711328.
10. Wang, W.; Cao, Z.; Elia, G.A.; et al. Recognizing the Mechanism of Sulfurized Polyacrylonitrile Cathode Materials for Li–S Batteries and beyond in Al–S Batteries. *ACS Energy Lett.* **2018**, *3*, 2899–2907. https://doi.org/10.1021/acsenergylett.8b01945.
11. Guo, Y.; Hu, Z.; Cui, Y.; et al. Al_2S_3 Cathode for Rechargeable Aluminum-Sulfur Batteries with Improved Cycling Reversibility. *Batter. Supercaps* **2022**, *5*, e202100355. https://doi.org/10.1002/batt.202100355.
12. Klimpel, M.; Kovalenko, M.V.; Kravchyk, K.V. Advances and challenges of aluminum–sulfur batteries. *Commun. Chem.* **2022**, *5*, 77. https://doi.org/10.1038/s42004-022-00693-5.
13. Deka, N.; Dutta, G.K. Recent advancement in carbon-based materials as sulfur hosts for rechargeable aluminum–sulfur (Al–S) batteries. *Curr. Opin. Electrochem.* **2023**, *38*, 101222. https://doi.org/10.1016/j.coelec.2023.101222.
14. Faheem, M.; Hussain, A.; Ali, M.; et al. Recent Theoretical and Experimental Advancements of Aluminum-Sulfur Batteries. *Chem. Rec.* **2024**, *24*, e202300268. https://doi.org/10.1002/tcr.202300268.
15. Zhang, Y.; Ma, L.; Tang, R.; et al. The host hollow carbon nanospheres as cathode material for nonaqueous room-temperature Al–S batteries. *Int. J. Hydrogen Energy* **2021**, *46*, 4936–4946. https://doi.org/10.1016/j.ijhydene.2020.11.076.
16. Smajic, J.; Wee, S.; Simoes, F.R.F.; et al. Capacity Retention Analysis in Aluminum-Sulfur Batteries. *ACS Appl. Energy Mater.* **2020**, *3*, 6805–6814. https://doi.org/10.1021/acsaem.0c00921.

17. Zheng, X.; Tang, R.; Zhang, Y.; et al. Design of a composite cathode and a graphene coated separator for a stable room-temperature aluminum–sulfur battery. *Sustain. Energy Fuels* **2020**, *4*, 1630–1641. https://doi.org/10.1039/c9se00762h.
18. Guo, Y.; Jin, H.; Qi, Z.; et al. Carbonized-MOF as a Sulfur Host for Aluminum–Sulfur Batteries with Enhanced Capacity and Cycling Life. *Adv. Funct. Mater.* **2019**, *29*, 1807676. https://doi.org/10.1002/adfm.201807676.
19. Guo, Y.; Hu, Z.; Wang, J.; et al. Rechargeable Aluminium–Sulfur Battery with Improved Electrochemical Performance by Cobalt-Containing Electrocatalyst. *Angew. Chem. Int. Ed.* **2020**, *59*, 22963–22967. https://doi.org/10.1002/anie.202008481.
20. Zhang, K.; Lee, T.H.; Cha, J.H.; et al. Two-dimensional boron nitride as a sulfur fixer for high performance rechargeable aluminum-sulfur batteries. *Sci. Rep.* **2019**, *9*, 13573. https://doi.org/10.1038/s41598-019-50080-9.
21. Xiao, X.; Tu, J.; Huang, Z.; et al. A cobalt-based metal–organic framework and its derived material as sulfur hosts for aluminum–sulfur batteries with the chemical anchoring effect. *Phys. Chem. Chem. Phys.* **2021**, *23*, 10326–10334. https://doi.org/10.1039/d1cp01232k.
22. Zheng, X.; Wang, Z.; Li, J.; et al. Binder-free S@$Ti_3C_2T_x$ sandwich structure film as a high-capacity cathode for a stable aluminum-sulfur battery. *Sci. China Mater.* **2022**, *65*, 1463–1475. https://doi.org/10.1007/s40843-021-1913-4.
23. Ai, Y.; Wu, S.C.; Zhang, F.; et al. Bifunctional TiN@N-doped-graphene catalyst based high sulfur content cathode for reversible Aluminum-Sulfur batteries. *Energy Storage Mater.* **2022**, *48*, 297–305. https://doi.org/10.1016/j.ensm.2022.03.019.
24. Hu, Z.; Xie, S.; Guo, Y.; et al. Isolated Co single atoms in nitrogen-doped graphene for aluminum-sulfur batteries with enhanced kinetic response. *J. Energy Chem.* **2022**, *67*, 354–360. https://doi.org/10.1016/j.jechem.2021.10.010.
25. Wang, F.; Jiang, M.; Zhao, T.; et al. Atomically Dispersed Iron Active Sites Promoting Reversible Redox Kinetics and Suppressing Shuttle Effect in Aluminum–Sulfur Batteries. *Nano-Micro Lett.* **2022**, *14*, 169. https://doi.org/10.1007/s40820-022-00915-4.
26. Ju, S.; Ye, J.; Zhang, H.; et al. Recognizing the contrasting role of N, O dual-coordinated single-atom iron catalyst in Li−S and Al−S batteries. *Energy Storage Mater.* **2023**, *56*, 1–12. https://doi.org/10.1016/j.ensm.2023.01.002.
27. Ju, S.; Yuan, C.; Zheng, J.; et al. Identifying single-atom catalysts for boosted Al–S conversion reactions. *Energy Storage Mater.* **2022**, *52*, 524–533. https://doi.org/10.1016/j.ensm.2022.08.030.
28. Lv, J.; Lai, G.; Yang, T.; et al. Enabling long cycle aluminum-sulfur batteries via structurally stable Co, N-doped graphene-CNTs covalently bonded hybrid. *Chem. Eng. J.* **2024**, *494*, 152811. https://doi.org/10.1016/j.cej.2024.152811.
29. Sun, Q.; Chai, L.; Yang, X.; et al. Hollow tubular sea-urchin structure with high catalytic activity of $NiCo_2Se_4$@CS_2 cathodes for high-performance Al/S batteries. *J. Colloid Interface Sci.* **2025**, *677*, 284–292. https://doi.org/10.1016/j.jcis.2024.08.071.
30. Gorle, M.; Jetti, V.R. Enhanced reliability of aluminum–sulfur batteries with cost-effective ionic liquid electrolyte and sulfur/graphite cathode. *New J. Chem.* **2024**, *48*, 4020–4029. https://doi.org/10.1039/d3nj05853k.
31. Zhang, X.; Tong, Y.; An, J.; et al. Local electronic regulation of single-atom catalysts to accelerate aluminum-sulfur conversion kinetics. *J. Energy Storage* **2025**, *129*, 117320. https://doi.org/10.1016/j.est.2025.117320.
32. Yu, G.; Liu, X.; Huang, W.; et al. Ferromagnetic Atomic d-p Orbital Hybridization for Promoting Al-S Batteries. *Adv. Mater.* **2025**, *37*, 2418784. https://doi.org/10.1002/adma.202418784.
33. Zhou, Q.; Zhang, X.; Wu, Y.; et al. Polyoxometalates@Metal-Organic Frameworks Derived Bimetallic Co/Mo_2C Nanoparticles Embedded in Carbon Nanotube-Interwoven Hierarchically Porous Carbon Polyhedron Composite as a High-Efficiency Electrocatalyst for Al–S Batteries. *Small* **2023**, *19*, 2304515. https://doi.org/10.1002/smll.202304515.
34. Lin, Z.; Mao, M.; Lv, T.; et al. Electroactive-catalytic conductive framework for aluminum-sulfur batteries. *Energy Storage Mater.* **2022**, *51*, 266–272. https://doi.org/10.1016/j.ensm.2022.06.055.
35. Liang, J.; Yin, L.; Tang, X.; et al. Kinetically Enhanced Electrochemical Redox of Polysulfides on Polymeric Carbon Nitrides for Improved Lithium–Sulfur Batteries. *ACS Appl. Mater. Interfaces* **2016**, *8*, 25193–25201. https://doi.org/10.1021/acsami.6b05647.
36. Tao, X.; Wang, J.; Liu, C.; et al. Balancing surface adsorption and diffusion of lithium-polysulfides on nonconductive oxides for lithium–sulfur battery design. *Nat. Commun.* **2016**, *7*, 11203. https://doi.org/10.1038/ncomms11203.
37. He, J.; Hartmann, G.; Lee, M.; et al. Freestanding 1T MoS_2/graphene heterostructures as a highly efficient electrocatalyst for lithium polysulfides in Li–S batteries. *Energy Environ. Sci.* **2019**, *12*, 344–350. https://doi.org/10.1039/c8ee03252a.
38. Al Salem, H.; Babu, G.; Rao, C.V.; et al. Electrocatalytic Polysulfide Traps for Controlling Redox Shuttle Process of Li–S Batteries. *J. Am. Chem. Soc.* **2015**, *137*, 11542–11545. https://doi.org/10.1021/jacs.5b04472.
39. Wang, H.; Shu, Q.; Zhou, Z.; et al. Engineering NiCo single atom alloy on MXene as cascade catalyst for high-performance Li–S batteries. *Nano Res.* **2025**, *18*, 94907557. https://doi.org/10.26599/nr.2025.94907557.
40. Liu, J. Catalysis by Supported Single Metal Atoms. *ACS Catal.* **2017**, *7*, 34–59. https://doi.org/10.1021/acscatal.6b01534.
41. Hu, P.; Wu, Y.F.; Gao, X.P.; et al. N/O dual coordination of cobalt single atom for fast kinetics sodium-sulfur batteries. *Rare Met.* **2025**, *44*, 288–299. https://doi.org/10.1007/s12598-024-02975-4.
42. Du, Z.; Chen, X.; Hu, W.; et al. Cobalt in Nitrogen-Doped Graphene as Single-Atom Catalyst for High-Sulfur Content Lithium–Sulfur Batteries. *J. Am. Chem. Soc.* **2019**, *141*, 3977–3985. https://doi.org/10.1021/jacs.8b12973.

43. Zhang, L.; Liu, D.; Muhammad, Z.; et al. Single Nickel Atoms on Nitrogen-Doped Graphene Enabling Enhanced Kinetics of Lithium–Sulfur Batteries. *Adv. Mater.* **2019**, *31*, 1903955. https://doi.org/10.1002/adma.201903955.
44. Liu, H.H.; Xu, Q.; Liu, H.; et al. P doping adjusts the coordination structure of single atoms to accelerate the catalytic bidirectional redox reaction in Li–S batteries. *Rare Met.* **2025**, *44*, 5428–5438. https://doi.org/10.1007/s12598-025-03233-x.
45. Liu, K.; Wang, L.; Chen, W.; et al. The roadmap of carbon-based single-atom catalysts: Rational design and electrochemical applications. *Rare Met.* **2025**, *44*, 7987–8132. https://doi.org/10.1007/s12598-025-03477-7.
46. Yang, S.; Wang, M.; Zhang, Y.; et al. Single-Molecule Confinement Induced Intrinsic Multi-Electron Redox-Activity to Enhance Supercapacitor Performance. *Energy Environ. Mater.* **2023**, *6*, e12396. https://doi.org/10.1002/eem2.12396.
47. Jones, J.; Xiong, H.; DeLaRiva, A.T.; et al. Thermally stable single-atom platinum-on-ceria catalysts via atom trapping. *Science* **2016**, *353*, 150–154. https://doi.org/10.1126/science.aaf8800.
48. Ferrari, A.C.; Robertson, J. Interpretation of Raman spectra of disordered and amorphous carbon. *Phys. Rev. B* **2000**, *61*, 14095–14107. https://doi.org/10.1103/physrevb.61.14095.
49. Fei, H.; Dong, J.; Feng, Y.; et al. General synthesis and definitive structural identification of MN_4C_4 single-atom catalysts with tunable electrocatalytic activities. *Nat. Catal.* **2018**, *1*, 63–72. https://doi.org/10.1038/s41929-017-0008-y.
50. Li, H.; Meng, R.; Guo, Y.; et al. Reversible electrochemical oxidation of sulfur in ionic liquid for high-voltage Al−S batteries. *Nat. Commun.* **2021**, *12*, 5714. https://doi.org/10.1038/s41467-021-26056-7.
51. Wang, S.; Yu, Z.; Tu, J.; et al. A Novel Aluminum-Ion Battery: Al/$AlCl_3$-[EMIm]Cl/Ni_3S_2@Graphene. *Adv. Energy Mater.* **2016**, *6*, 1600137. https://doi.org/10.1002/aenm.201600137.
52. Yu, Z.; Kang, Z.; Hu, Z.; et al. Hexagonal NiS nanobelts as advanced cathode materials for rechargeable Al-ion batteries. *Chem. Commun.* **2016**, *52*, 10427–10430. https://doi.org/10.1039/c6cc05974k.
53. Li, H.; Yang, H.; Sun, Z.; et al. A highly reversible Co_3S_4 microsphere cathode material for aluminum-ion batteries. *Nano Energy* **2019**, *56*, 100–108. https://doi.org/10.1016/j.nanoen.2018.11.045.
54. Yang, J.; Jia, X.; Li, B.; et al. Precision-Engineered Nanocatalysts via Lattice Tailoring and d-Band Center Modulation for High-Performance Lithium-Sulfur Batteries. *Carbon Energy* **2025**, *7*, e70043. https://doi.org/10.1002/cey2.70043.
55. Jiang, B.; Tian, D.; Qiu, Y.; et al. High-Index Faceted Nanocrystals as Highly Efficient Bifunctional Electrocatalysts for High-Performance Lithium–Sulfur Batteries. *Nano-Micro Lett.* **2022**, *14*, 40. https://doi.org/10.1007/s40820-021-00769-2.
56. Guo, J.; Liang, H.; Yang, Q.; et al. Steric-Hindrance Effect Induced Fabrication of Lightweight, Bi-Functional, and Easy-to-Infiltrate Hosts for 502 Wh kg^{-1} Lithium-Sulfur Batteries. *Adv. Mater.* **2026**, *38*, e18154. https://doi.org/10.1002/adma.202518154.